Title

Bivalence Mn5O8 with hydroxylated interphase for high-voltage aqueous sodium-ion storage

Journal

Nature Communications, 7(1)

ISSN

2041-1723

Authors

Shan, Xiaoqiang

Charles, Daniel S

Lei, Yinkai

et al.

Publication Date

2016

DOI

10.1038/ncomms13370

Peer reviewed

nature COMMUNICATIONS

ARTICLE

Received 22 Apr 2016 | Accepted 27 Sep 2016 | Published 15 Nov 2016

DOI: 10.1038/ncomms13370 OPEN

Bivalence Mn_5O_8 with hydroxylated interphase for high-voltage aqueous sodium-ion storage

Xiaoqiang Shan[1,*], Daniel S. Charles[1,*], Yinkai Lei[2], Ruimin Qiao[3], Guofeng Wang[2], Wanli Yang[3], Mikhail Feygenson[4], Dong Su[5] & Xiaowei Teng[1]

Aqueous electrochemical energy storage devices have attracted significant attention owing to their high safety, low cost and environmental friendliness. However, their applications have been limited by a narrow potential window (~1.23 V), beyond which the hydrogen and oxygen evolution reactions occur. Here we report the formation of layered Mn_5O_8 pseudocapacitor electrode material with a well-ordered hydroxylated interphase. A symmetric full cell using such electrodes demonstrates a stable potential window of 3.0 V in an aqueous electrolyte, as well as high energy and power performance, nearly 100% coulombic efficiency and 85% energy efficiency after 25,000 charge–discharge cycles. The interplay between hydroxylated interphase on the surface and the unique bivalence structure of Mn_5O_8 suppresses the gas evolution reactions, offers a two-electron charge transfer via Mn^{2+}/Mn^{4+} redox couple, and provides facile pathway for Na-ion transport via intra-/inter-layer defects of Mn_5O_8.

[1] Department of Chemical Engineering, University of New Hampshire, Durham, New Hampshire 03824, USA. [2] Department of Mechanical Engineering and Materials Science, University of Pittsburgh, Pittsburgh, Pennsylvania 15261, USA. [3] Advanced Light Source, Lawrence Berkeley National Laboratory, Berkeley, California 94720, USA. [4] Chemical and Engineering Materials Division, Spallation Neutron Source, Oak Ridge National Laboratory, Oak Ridge, Tennessee 37831, USA. [5] Center for Functional Nanomaterials, Brookhaven National Laboratory, Upton, New York 11973, USA. * These authors contributed equally to this work. Correspondence and requests for materials should be addressed to X.T. (email: xw.teng@unh.edu).

Rechargeable aqueous electrochemical energy storage (EES) devices, especially ones using earth-abundant and non-toxic materials, have shown great promise for many applications owing to their high safety, low cost and environmental friendliness[1]. However, the thermodynamically stable potential window for aqueous EES has an intrinsic limit of 1.23 V, beyond which the hydrogen evolution reaction (HER) and oxygen evolution reaction (OER) occur. The evolved gas from electrolyte decomposition also severely deteriorates the electrode. A potential window of 1.23 V is too narrow for storage devices to achieve high energy and power performance.

Extensive efforts have been made to break this limit on the potential window while retaining the benefits of aqueous energy storage systems. One approach is to adjust the pH of the electrolyte to suppress HER and/or OER[1]. An aqueous battery of 2.8 V was reported by using basic electrolyte in the anode compartment (to decrease HER potential following Nernst equation) and acidic electrolyte in the cathode compartment (to increase OER potential)[2]. A Li-ion-conductive membrane was therefore needed to separate two compartments with the drastic pH difference. Another approach to suppress gas evolution is through utilization of solid–electrolyte interphase (SEI). Such interphase is ion-conductive and but not electron-conductive, protecting the electrode (for example, Li anode) from direct contact with water[3]. Recently, Suo *et al.* reported a water-in-salt electrolyte, by dissolving concentrated Li-bis(trifluoromethane sulfonyl)imide salt in water. This electrolyte system introduces a desirable SEI that enables an aqueous Li-ion full cell operation at 2.3 V for more than 1,000 cycles[4]. Although these excellent works open up the opportunities for improving the potential window, the intrinsic limitation of the ionic conductivity in Li-ion-based aqueous systems has hindered high-rate performance of the cell, especially for the pseudocapacitive storage.

Here we report a high-rate high-voltage aqueous Na-ion full cell system based on a surface hydroxylated Mn_5O_8 electrode. As probed by synchrotron-based surface-sensitive soft X-ray spectroscopy (sXAS), an ice-like surface hydroxyl layer is formed after cycling. Density functional theory (DFT) calculations show that the interplay between the hydroxylated interphase and the unique bivalence ($Mn^{2+}{}_2Mn^{4+}{}_3O_8$) layered structure suppresses the HER and OER with a stable potential window of 3.0 V. The system exhibits a two-electron charge transfer via Mn^{2+}/Mn^{4+} redox couple, and provides facile pathway for Na-ion transport at high rate. The 3.0 V aqueous symmetric full cell exhibits a high energy density, 23 Wh kg^{-1} at a rate of 550 C, with nearly 100% coulombic efficiency and 85% energy efficiency after 25,000 charge–discharge cycles.

Results

Synthesis and characterizations of Mn_5O_8 nanoparticles. Mn_5O_8 is the only bivalent manganese oxide that has a layered structure[5]. Although Mn_5O_8 has abundant interlayer and intralayer defects for facile ionic transport, its capability for energy storage has rarely been reported. In this work, Mn_5O_8 nanoparticles were synthesized by heating Mn_3O_4 nanoparticles at 270 °C for 2 h in the open air. X-ray and neutron pair distribution function (PDF) analyses, shown in Fig. 1a,b, point to the formation of monoclinic Mn_5O_8 (Supplementary Tables 1 and 2), which consists of two-dimensional octahedral sheets of $[Mn_3^{4+}O_8]$ in the *bc* plane separated by Mn^{2+} layers, giving a compositional formula of $Mn^{2+}{}_2Mn^{4+}{}_3O_8$. Half of the Mn^{4+} sites in the main octahedral sheets are not fully occupied, above and below these vacant sites are Mn^{2+} sites (Fig. 1c). Apart from the major component Mn_5O_8, a small amount of Mn_3O_4 is present as seen in both the X-ray diffraction (Supplementary Fig. 1) and PDF analyses. Transmission electron microscopy (TEM) and scanning TEM showed that Mn_5O_8 particles have an average size of 19 nm and possess a highly crystalline monoclinic structure (Fig. 1d,e)[5]. X-ray photoelectron spectroscopy (XPS)

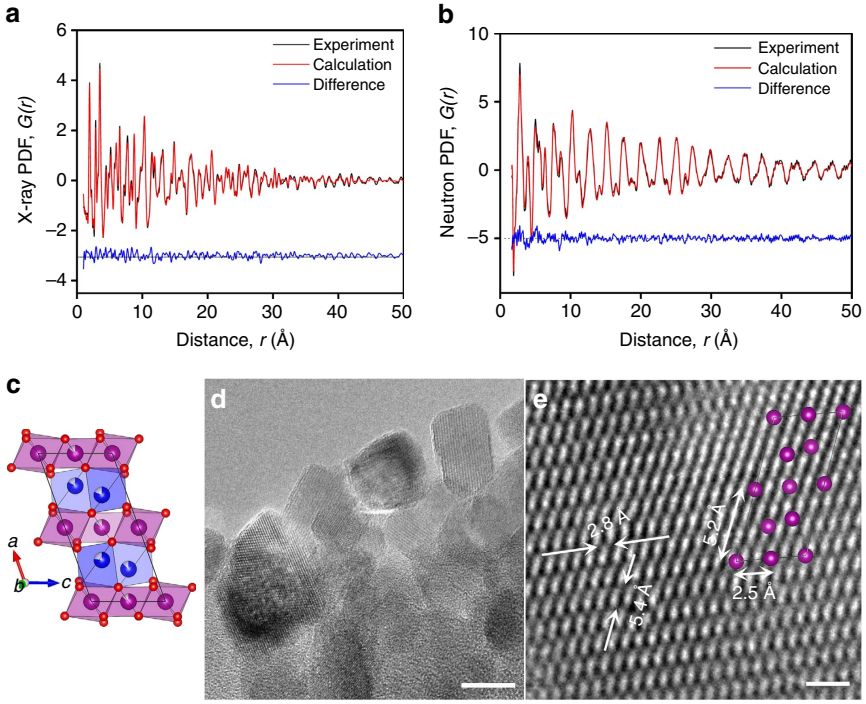

Figure 1 | Structure characterizations of Mn_5O_8 nanoparticles. (**a**) X-ray and (**b**) neutron PDF analyses of Mn_5O_8 nanoparticles. (**c**) Lattice structure of Mn_5O_8 (purple: Mn^{4+}; blue: Mn^{2+}; red: O; white: probability of unoccupied site) obtained from PDF fitting; (**d**) TEM and (**e**) STEM images of Mn_5O_8 nanoparticles (inset showed Mn_5O_8 lattice (Mn only) along <010> direction). Scale bars, 20 nm (**d**) and 1 nm (**e**), respectively.

was used to analyse the surface of Mn_5O_8 nanoparticles, where only manganese, oxygen, carbon and trace sodium signals can be detected without other surface residuals from synthesis and processing (Supplementary Fig. 2). XPS data show that Mn^{2+} and Mn^{4+} valences in both 2p and 3s chemical states. The XPS spectra are fitted to Mn 3 s doublets, which are split by 5.7 eV (Mn^{2+}) and 4.5 eV (Mn^{4+}), respectively. The integrated intensity ratio of Mn^{2+} and Mn^{4+} is calculated to be around 1:2, close to that of theoretical value from Mn_5O_8 at near surface.

Electrochemical studies of Mn_5O_8. Figure 2a shows the cyclic voltammetry (CV) curves of the Mn_5O_8-based electrodes. The Mn_5O_8 material was mixed with carbon black at mass ratio of 7:3. The CV measurements were conducted using a three-electrode half-cell using a 0.1 M Na_2SO_4 electrolyte and a mercury sulfate electrode (MSE) as reference electrode. The CVs of carbon black show Mn_5O_8 material is the major contributor to the overall capacitance (Supplementary Fig. 3). The Mn_5O_8 nanoparticles show a wide potential window between -1.7 V (corresponding to overpotential of 0.64 V towards HER) and 0.8 V (corresponding to overpotential of 0.63 V towards OER), demonstrating the high resistance to gas evolution reactions. To our knowledge, this is the first demonstration for a stable 2.5 V potential window in an aqueous Na-ion half-cell. Moreover, the resistive capability of the Mn_5O_8 electrode towards HER and OER can also be demonstrated by analyzing the reaction kinetics of HER and OER using TAFEL plots (Supplementary Fig. 4). The results show that Mn_5O_8 has sluggish HER and OER kinetics, demonstrated by high TAFEL slopes at various scan rates, compared with various commercial Mn_3O_4 and Co_3O_4 nanopowders (Supplementary Fig. 5).

Figure 2a also shows nearly reversible current–voltage curves with discernable redox peaks from 1 to 1,000 mV s^{-1}, suggesting mixed contributions from pseudocapacitive and redox processes. There are noticeable peak shifts (blue arrows) with scan rates and peak separation between anodic and cathodic scans. The peak separation increases with scan rates but in a considerably less extent compared with battery materials. The increased peak separation is typically attributed to a higher overpotential that is required to transport the ions at faster rates. Therefore, the less-distinct peak separation here indicates that our system has the potential for high-power capability with facile Na-ion transport[6]. In addition to neutral electrolyte, CVs of Mn_5O_8 electrodes were also conducted in Na_2SO_4-based electrolytes with different pH values, showing very similar behaviour in the CVs and gravimetric capacitances at the various scan rates (Supplementary Fig. 6).

Current–voltage relationship provides insight into the charge-storage mechanism. Assuming that the current (i) obeys the power law relationship with scan rate (v) at a given potential, and can be expressed as a combination of surface-controlled capacitive effects ($i_1 = k_1 v$) and diffusion-controlled Na-ion intercalation ($i_2 = k_2 v^{1/2}$) (ref. 7):

$$i = k_1 v + k_2 v^{1/2} \quad \text{or} \quad i/v^{1/2} = k_1 v^{1/2} + k_2 \qquad (1)$$

Plotting $i/v^{1/2}$ versus $v^{1/2}$ curves at a given potential, allows for the calculation of k_1 and k_2. Thus, the contributions from capacitive charge and diffusion-limited redox charge during the CV cycling are extracted quantitatively (Fig. 2b and Supplementary Figs 7 and 8). Figure 2c compares the capacitive contribution of Mn_5O_8 nanoparticles with Mn_5O_8 and Mn_3O_4 bulk materials, as well as Mn_3O_4 nanoparticles that are similar in size (18 nm) to the Mn_5O_8 nanoparticles. Mn_3O_4 is chosen since it has a bivalent structure ($Mn^{2+}Mn^{3+}{}_2O_4$) analogous to that of Mn_5O_8 ($Mn^{2+}{}_2Mn^{4+}{}_3O_8$). Figure 2c shows that Mn_5O_8 nanoparticles have a greater contribution from capacitive storage compared with other materials. The results suggest that Mn_5O_8 nanoparticles behave as a pseudocapacitive material due to high ratio of capacitive contribution for the charge stored, as well as its unique layered structure for facile Na-ion transport.

Symmetric full cells were assembled to evaluate the electrochemical performance of Mn_5O_8. Each electrode was prepared by depositing Mn_5O_8 (5 mg) and carbon black (1.25 mg) on carbon paper current collector (1.77 cm^2), yielding a thickness of $\sim$80 µm. With 1 M Na_2SO_4 electrolyte, Mn_5O_8 cell displays a stable potential window of 3.0 V after 2,000 charge and discharge cycles, the largest stable potential window ever reported for an aqueous storage device. Nearly linear potential-capacity curves, characteristic of a pseudocapacitive response, are observed (Fig. 3a). When current densities increase from 5 to 50 A g^{-1}, discharge times evolve from $\sim$42 s (corresponding to a rate of 85.7 C) to 0.75 s (a rate of 4,800 C), and electrode capacities change from 116 to 20 mAh g^{-1} accordingly. Figure 3b shows charge and discharge potential-capacity curves at various current densities (Supplementary Fig. 9). The discharge curve is lower than charge curve, reflecting the charge and energy losses during cycling. Coloumbic and energy efficiencies, the ratio of the amount of charge and energy that are taken from the device versus the amount that was stored during each cycle, are shown in Fig. 3b inset after 2,000 cycles. When current density increases from 5 to 50 A g^{-1}, coloumbic efficiency of Mn_5O_8 electrode remains nearly 100%, and energy efficiency increases from 80 to 97%. Figure 3c shows good cycling stability of Mn_5O_8 full cells at

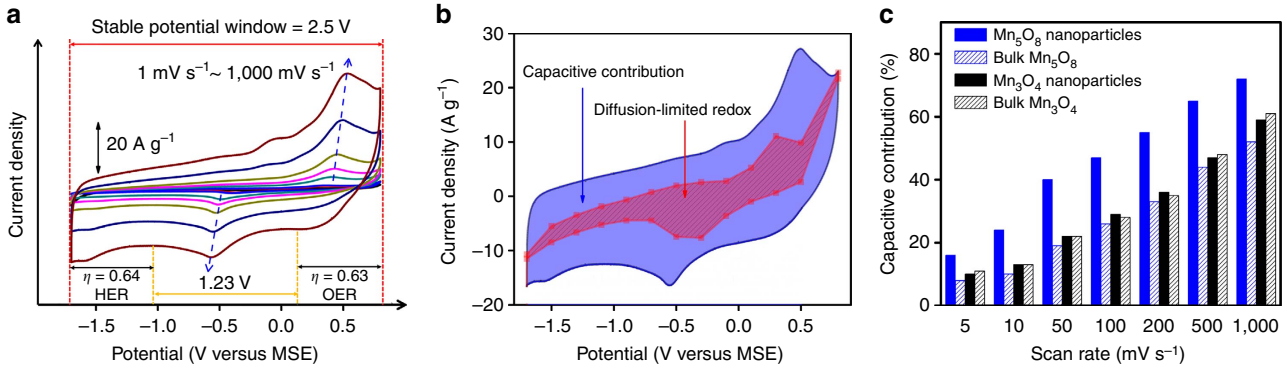

Figure 2 | Electrochemical measurements of Mn_5O_8 electrodes in a half-cell. (**a**) CVs show a stable potential window of 2.5 V and large overpotential (η) towards HER and OER. (**b**) Electro-kinetics study of CV at 500 mV s^{-1}. The contributions from capacitive process (blue) and diffusion-limited redox process (red) are shaded. (**c**) Capacitive contribution to the total charge stored at various scan rates in Mn_5O_8 and Mn_3O_4 nanoparticles and bulk materials.

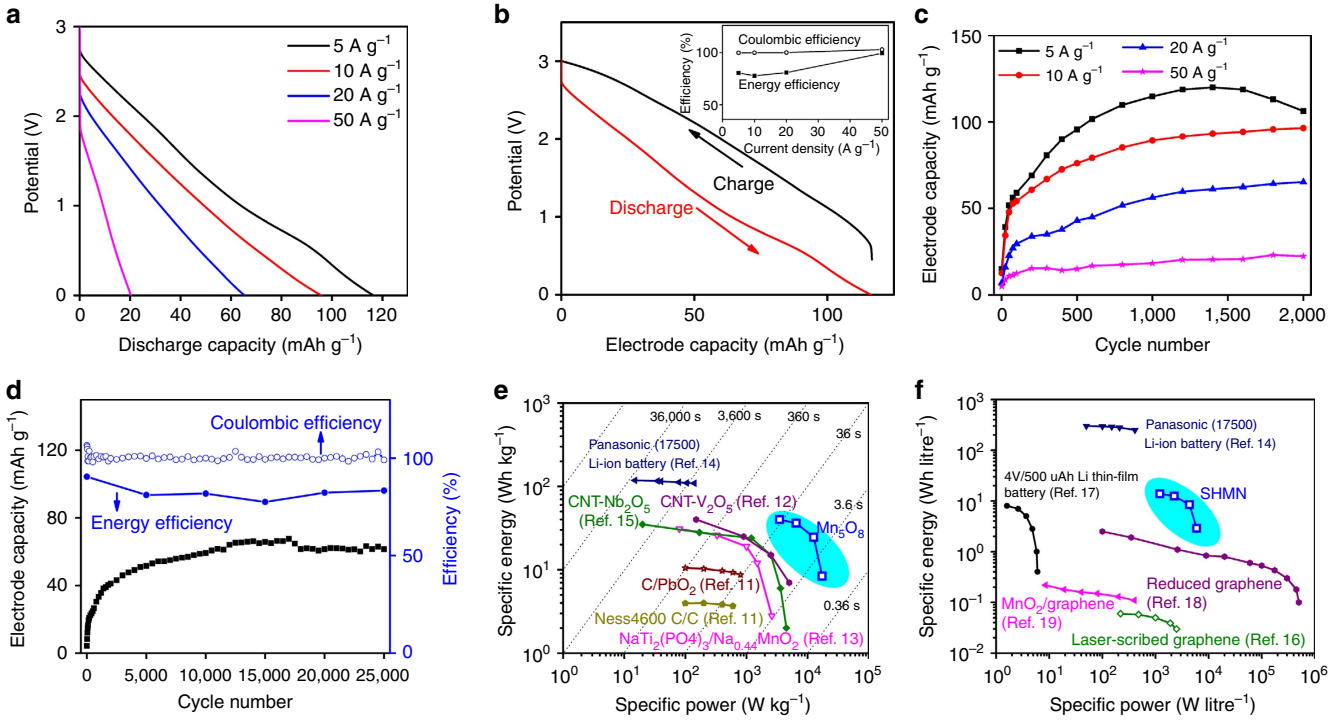

Figure 3 | Electrochemical tests of Mn_5O_8symmetric cells. (**a**) Discharge capacity of Mn_5O_8 electrode as a function of current density; (**b**) electrode capacity during charge and discharge processes at 5 A g^{-1} (inset: energy and coloumbic efficiencies from 5 to 50 A g^{-1}). (**c**) Electrode capacity as a function of cycle; (**d**) Electrode capacity and coloumbic efficiencies as functions of cycle at 20 A g^{-1}. (**e**) Gravimetric and (**f**) volumetric energy and power densities of Mn_5O_8 cell compared with other aqueous (open symbols) and non-aqueous (solid symbols) devices. (**e**) Reported to the mass of electrode materials except Panasonic (17,500) Li-ion battery and Ness4600 C/C. (**f**) Reported to the volume of whole device. A packaging factor of 0.4 was used for Mn_5O_8 cell since its volumetric energy and power densities are calculated based on the volume of electrode material. The results are obtained after 2,000 charge–discharge cycles unless specified otherwise.

a 3.0 V potential window from 5 to 50 A g^{-1}. At 20 A g^{-1}, the Mn_5O_8 cell shows excellent coloumbic efficiency (~100%) and energy efficiency (~85%), and a plausible electrode capacity of 61 mAh g^{-1} after 25,000 cycles (Fig. 3d). High coulombic and energy efficiencies, good linearity between potential and electrode capacity, as well as superior cycling stability, all suggest that Mn_5O_8 acts as a stable pseudocapacitive material at high rate.

Low-rate performance of Mn_5O_8 cell was also studied. At low current densities, electrode capacity fades rapidly (Supplementary Fig. 10). This result indicates Mn_5O_8 acts closer to a batteries-like electrode materials at low-rate, during which storage capacity is contributed significantly from diffusion-limited redox process. This is confirmed by non-linear voltage-capacity curves at low rate, exhibiting voltage plateaus (Supplementary Fig. 11), concurrent with the results obtained from CV measurements in half-cell showing that diffusion-limited redox process contributed predominately to the overall charge stored at low scan rates (Fig. 2c). The fact, that Mn_5O_8 electrode capacities show an optimal performance at a current density of 5 A g^{-1} and fade remarkably at the low current densities (for example, 0.5 and 1 A g^{-1}) in the prolonged cycles, could also be attributed to a parasitic reaction from either hydrogen or oxygen evolution occurring at low rates. The resulting gas evolution could deteriorate the Mn_5O_8 electrode and cause the loss of capacity at prolonged cycles. It has also been pointed out that though electrode material contains Mn_3O_4 impurity phase (<20%), it shows very sluggish electro-kinetics of HER and OER as shown in TAFEL plots and slopes (Supplementary Figs 4 and 5), indicating high overpotential towards HER and OER at off-equilibrium electrochemical process at high rates. On the other hand, at low rates (0.5 and 1 A g^{-1}), parasitic reaction from gas evolution, possibly catalysed by Mn_3O_4 impurity phase, may occur in near-equilibrium condition and deteriorate the electrode materials.

Mn_5O_8 electrode materials show relatively low discharge capacities in the initial cycles, and then the capacities continuously increase before showing steady fades for the rest of the cycles. Although similar behaviours have been reported in several electrode systems[8–10], the exact mechanism of the capacity increase in the initial cycling is still unclear. It has been suggested that initial cycling may help the electrode materials reach their optimal condition by facilitating the ionic transport[9]. We believe our Mn_5O_8 electrode may undergo a similar prolonged-conditioning process during the initial cycling, reflected by the overall electrical resistance of the button-cell as calculated by *i*–*R* drop during the discharge processes. Our data show that the cell resistances decrease during the initial cycles and eventually become relatively stable and then start to increase again (Supplementary Fig. 12). Correspondingly, electrode capacities show nearly opposite trends compared with cell resistances: the discharge capacities start to increase at initial cycles in a continuous manor and then show a steady fading for the rest of cycles. We have also pre-soaked the electrode materials in Na_2SO_4 electrolyte before cell assembling in order to improve ionic transport at electrode and electrolyte interface. However, it shows that electrode capacities appear very similar trends to those shown in Fig. 3c (Supplementary Figs 10 and 13). The results indicate that Na-ions transport within Mn_5O_8 materials during the initial cycling accounts for the large cell resistance.

Figure 3e shows that Mn_5O_8 symmetric cells exhibit gravimetric energy and power densities up to 40 Wh kg^{-1} and

17,400 W kg^{-1}; and even more impressively, exhibit volumetric energy and power densities of ~13 Wh l^{-1} and 6,000 W l^{-1} (Fig. 3f). These values, obtained after 2,000 cycles, are much higher than those of several aqueous and even non-aqueous devices found in commercial products (less than five cycles) and recent literature in terms of gravimetric performance[11–15], and volumetric performance[16–20]. Our Mn_5O_8 electrode materials show very competitive performance for aqueous electrochemical energy storage especially at high rates as compared with other Mn-based electrode materials reported previously (Supplementary Table 3). Further increasing the energy density of the Mn_5O_8 electrode, especially at low current densities, will be important to develop high-performance aqueous EES devices that could rival their non-aqueous counterparts.

Discussion

In order to elucidate the mechanisms of this high-voltage and high-rate performance found in the Mn_5O_8 system, we first provide synchrotron-based sXAS results with its inherent surface and elemental sensitivities, followed by the DFT calculations.

First, probing the formation of interphase on the surface of Mn_5O_8 is not trivial. As most electrode–electrolyte interphases are amorphous, STEM fails to detect the interphase layer (Supplementary Fig. 14). We also carried out neutron PDF analyses on the Mn_5O_8 nanoparticles before and after cycling in Na_2SO_4 and D_2O solution. Although Mn_5O_8 nanoparticles were prepared in the heavy water (D_2O) and tested for neutron scattering under an inert gas environment, light water (H_2O) residuals that might be introduced from moisture in the air showed much strong scattering, so that neutron PDF analysis was unable to identify any interphase on surface of Mn_5O_8 materials (Supplementary Fig. 15). Fortunately, surface and elemental sensitivity could be achieved by synchrotron-based soft X-ray spectroscopy through the electron-decay channel[21]. In sharp contrast to neutron scattering, sXAS measurement was conducted in the ultra-high vacuum condition, so that weakly adsorbed water molecules (physically adsorbed or dissociatively adsorbed water) were completely removed and only strongly bonded molecules (for example, interphase) remained on surface. In particular, it has been well established that the hydroxyl group could be probed in water and organic molecules through oxygen K-edge sXAS, with two features at ~535 and 537 eV from the unsaturated H-bonds, known as the 'water pre-edge' and 'water main-peak', respectively[22–25]. In addition, another post-edge hump above 540 eV is from the saturated H-bonds, especially visible in ice[23]. Figure 4a is the O-K sXAS results collected on the pristine and cycled Mn_5O_8 electrodes with a surface probe depth of 10 nm. It is evident that, upon cycling, Mn_5O_8 electrode displays both the fingerprinting water-features at the 535 and 537 eV. These features resemble exactly the 'pre-edge' and 'main peak' from water. Therefore, the strong spectral lineshape contrast between the pristine and the cycled electrode evidently indicates the formation of hydroxylated species on the electrode surface upon cycling. Moreover, the O–K features between 528 and 534 eV represents the spectroscopic excitations to the hybridized state of O-2*p* and Mn-3*d*, which are split by the crystal field of the local Mn–O coordination geometry[26]. A clear loss of intensity on this hybridization feature is observed after cycling. This intensity loss is further proof of the change of the Mn–O coordination on the surface and is consistent with the formation of hydroxyl group that covers the surface of the electrode.

Due to the great sensitivity of the sXAS lineshape to the hydroxyl structure, the O–K spectra reveals a very interesting molecular arrangement of the hydroxyl groups on the surface of Mn_5O_8 electrode. Because the Mn-3*d*/O-2*p* hybridization features between 528 and 534 eV are purely from Mn_5O_8 contribution, we can normalize the spectral intensity to these features and subtract the Mn_5O_8 (pristine) signal from the after-cycling data to obtain the surface hydroxyl signal. The spectrum of the obtained surface hydroxyl signal is plotted in Fig. 4b (purple). It is clear that the surface hydroxyl layer is different from ice, missing the high energy hump from the saturated H-bonds in ice[23]. It reproduces the 'pre-peak' and 'main peak' of liquid water[22,23], with the 'main peak' at 537.5 eV dominating the spectrum. The enhancement of this main peak has been predicted by theoretical calculations[23], which stems from a combination of an extended O–O distance and perfectly aligned H-bonds along the O–O direction. The calculation result of the O–O distance of 3.50 Å with such a well-aligned H-bond is shown in Fig. 4b for comparison. Therefore, the O–K sXAS not only evidently shows that a hydroxyl layer is formed on the surface of the Mn_5O_8 electrodes after cycling, it also indicates a striking ordering of the absorbed molecules, with perfectly aligned H-bonds along O–O direction, like that in ice, but with a much longer distance between the O atoms. Although the underlying mechanism of the formation of hydroxylated interphase is still unclear, we believe it is largely

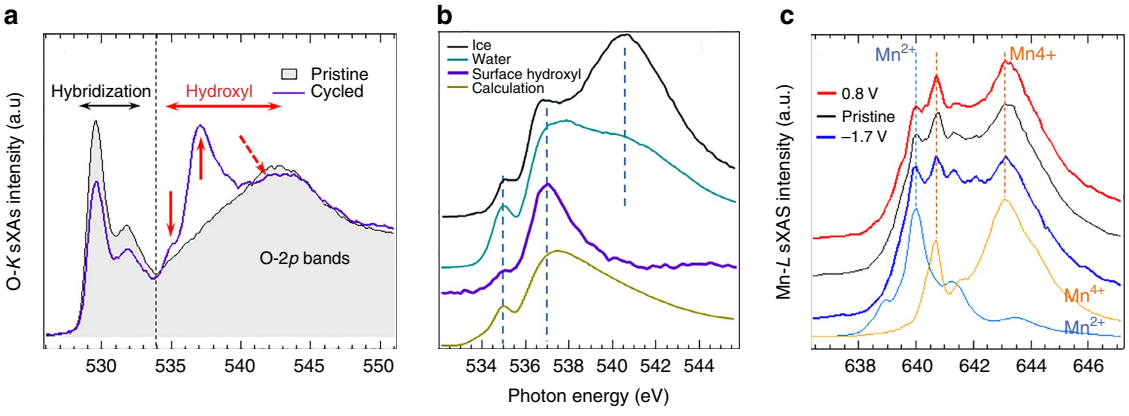

Figure 4 | sXAS analysis of surface hydroxylated Mn_5O_8. (**a**) O-K sXAS of Mn_5O_8 (pristine) and Mn_5O_8 electrode after two CV cycles between −1.7 and 0.8 V. Features below 534 eV are from the hybridization of Mn-3*d* and O-2*p* states. The 535 and 537 eV peaks are fingerprints of the water 'pre-peak' and 'main peak'. (**b**) A comparison of the O-K sXAS of the surface hydroxyl layer of Mn_5O_8 with water[22], ice[23] and one of the calculations with aligned H-bonds but lengthened O–O (3.50 and 3.00 Å) distances (Fig. 3a–g in ref. 23). (**c**) Mn *L*-edge of Mn_5O_8 (pristine) and Mn_5O_8 at different electrochemical cycling stages along with references from MnO (blue) and Li_2MnO_3 (yellow).

due to the interaction between Mn_5O_8 surface and water during the electrochemical cycling since no hydroxylated interphase is observed in the pristine Mn_5O_8 material (Fig. 4a). DFT calculations show that Mn^{2+} terminated (100) surface of Mn_5O_8 has a lower surface energy ($0.87\,J\,m^{-2}$) than Mn^{4+} terminated (100) surface ($1.80\,J\,m^{-2}$). Therefore, the interaction between Mn^{2+} and water during the electrochemical cycling might account for the formation of hydroxylated interphase on the Mn^{2+} terminated (100) surface of Mn_5O_8.

Second, the charge-storage mechanism is revealed by the Mn L-edge sXAS measurements (Fig. 4c). Mn-L sXAS is a direct probe of the Mn-3*d* electron states, so the spectral lineshape is very sensitive to the normal valence of Mn[27,28]. Figure 4c shows the Mn L-edge sXAS data collected on the Mn_5O_8 and the reference samples with Mn^{2+} (MnO) and Mn^{4+} (Li_2MnO_3) valences. The spectra show that the Mn_5O_8 electrode material is composed of Mn^{4+} (641 and 643.5 eV), Mn^{2+} (640 eV) and a trace amount of Mn^{3+}, supporting the coexistence of Mn_5O_8 phase and trace Mn_3O_4 phases. The changes of peak intensity at 640 eV (Mn^{2+}), 641 eV (Mn^{4+}) and 643.5 eV (Mn^{4+}) fingerprints the evolution of oxidation states of Mn with cycling. The Mn_5O_8 electrode at a reduced state (-1.7 V) displays a high-intensity ratio of Mn^{2+} to Mn^{4+}, while this ratio decreases at the oxidized state (0.8 V), suggesting the transition from Mn^{2+} to Mn^{4+} during oxidation processes. It is therefore evident that a two-charge transfer reaction via Mn^{2+}/Mn^{4+} redox couple can be achieved in the layered Mn_5O_8 system, indicating a great potential for high-capacity energy storage.

Furthermore, the mechanistic understanding of the resistive capability of surface-hydroxylated Mn_5O_8 towards HER and OER is obtained through a comparative DFT calculation on the surfaces of hydroxylated Mn_5O_8, pure Mn_5O_8 and Mn_3O_4. The Mn^{2+} terminated (100) surface of Mn_5O_8 is considered for the study, since our calculation predicted that Mn^{2+} terminated (100) surface had a lower surface energy ($0.87\,J\,m^{-2}$) than Mn^{4+} terminated (100) surface ($1.80\,J\,m^{-2}$). Figure 5 compares water splitting at various potential windows. Nearly all the water splitting steps are energetically unfavourable at zero potential; at a potential of 1.23 V (equilibrium potential of water splitting), all reaction steps are exothermic on three surfaces, except for OH dissociation on hydroxylated Mn_5O_8. The limiting potential at which all reaction steps become exothermic is determined to be 1.86, 1.64 and 1.68 V for hydroxylated Mn_5O_8, Mn_5O_8 and Mn_3O_4, respectively, indicating hydroxylated interphase increases the energy barriers for water splitting. The activation energy of each intermediate reaction steps during the HER and OER on the three surfaces was showed (Supplementary Fig. 16). The activation energy of the rate-determining step is all substantially higher for OER, indicating that OER is intrinsically difficult on all three surfaces. The activation energy of water dissociation, limiting step of HER, follows the order of hydroxylated Mn_5O_8 (1.41 eV) > Mn_5O_8 (0.45 eV) > Mn_3O_4 ($\sim$0 eV). Hydroxylated Mn_5O_8 possesses an activation energy $\sim$1 eV higher than that of Mn_3O_4, implying that the reaction rate at room temperature (300 K) is at least 17 orders of magnitude slower according to the Arrhenius equation. Therefore, the DFT calculations directly support the experimental observation of high overpotential (>0.6 V) towards HER and OER for the hydroxylated Mn_5O_8. It was recently reported that Mn_5O_8 nanoparticles showed very good OER activity in a neutral electrolyte in the presence of Mn^{3+} species[29]. Further studies will be needed to elucidate the influence of Mn valences, such as Mn^{3+} (from Mn_3O_4 or Mn_2O_3 phase) or Mn^{2+}/Mn^{4+} (from Mn_5O_8), on the gas evolution reactions.

This work shows that an unprecedented potential window of 3.0 V in aqueous Na-ion system can be achieved through the use of surface hydroxylated Mn_5O_8 electrodes. Gas evolution reactions are effectively inhibited through the interplay between the Mn^{2+} terminated surface and hydroxylated interphase. In addition, the superior power performance of Mn_5O_8 cell can be attributed to the unique layered, bivalence structure of Mn_5O_8 that enables facile Na-ion transport. In general, the ion transport through the electrode and electrolyte interface is critical for the rate performance of energy storage devices. Typical approaches to mitigate the transport barrier include decreasing the dimension of electrode materials to nanoscale, designing functional layered structure for facile ion intercalation, coating secondary conductive material on electrode surface, or developing cation-disordered electrode materials with decreased energy barrier for ion transport[6,8,30–32]. Mn^{2+} terminated (100) surface of Mn_5O_8 has plenty of unoccupied sites, and hence provides natural tunnels for Na-ion transport along <100> direction (black arrows) (Supplementary Fig. 17). Through the surface-sensitive soft X-ray spectroscopy, we also reveal the formation of a strikingly ordered ice-like surface hydroxyl layer but with much longer O–O distance after cycling. It is also possible that such a hydroxylated coating on the surface of Mn_5O_8 modifies the interaction between Na-ion with Mn_5O_8 by facilitating the electrostatic interaction between Na-ion and hydroxyl oxygen (red arrow). Although the electrochemical properties of Mn_5O_8 have been largely overlooked since its structure was determined in 1965 (ref. 5), our result shows that Mn_5O_8, the only bivalence layered manganese oxide, may serve as a new generation of pseudocapacitor electrode materials for enabling a stable potential window of 3.0 V for aqueous energy storage. Our results may offer a new paradigm for developing electrode materials with a wide potential window and facile charge transfer for aqueous energy storage devices, which exhibits

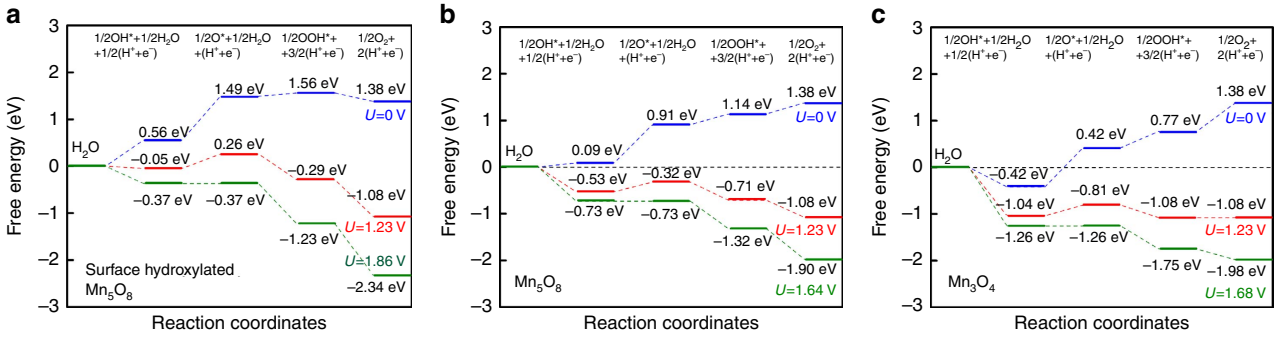

Figure 5 | DFT calculations. The free energy evolution for water splitting steps at different potentials on surfaces of (**a**) surface hydroxylated Mn_5O_8, (**b**) pure Mn_5O_8 and (**c**) Mn_3O_4 predicted from DFT.

the performance comparable to that of non-aqueous Li-ion batteries, but much safer, less costly and more environmentally benign. In addition, it will be an interesting topic for further studies on whether and how a well ordered hydroxylated interphase could form on the surface of other metal oxides, increase their overpotential towards gas evolution reactions, and therefore increase the potential window of aqueous energy storage.

Methods

Materials synthesis. Synthesis was conducted in a magnetically-stirred 50 ml reaction batch of 25.3 mM $MnCl_2 \cdot 4H_2O$ (Alfa Aesar, 99% metals basis) dissolved in 14 ml deionized water (DI H_2O) (18.2 MΩ; Millipore, Inc.) at room temperature under an open environment. A 20 ml syringe was used to controllably inject a solution of 0.3 M NaOH (Alfa Aesar, 99.99% metals basis) into $MnCl_2$ solution at a constant flow rate of 0.167 ml min^{-1} for 50 min using a computer-controlled syringe pump (New Era Syringe Pumps, Inc.). The resulting dark-brown precipitate was permitted to ripen for an additional 30 min at room temperature with stirring. The product was then washed thoroughly with DI H_2O and ethanol, vacuum-dried and then heated at 270 °C for 2 h.

Electrochemical tests. The anodic electrochemical properties of the Mn_5O_8 product were studied via a three-electrode half-cell, which contained a rotating glassy carbon electrode (Pine Instrument Company) as the working electrode, a platinum wire counter electrode and mercury sulfate (saturated K_2SO_4) reference electrode (MSE). The electrochemical half-cell was powered by single-channel electrochemical workstation (Model 600D, CH Instruments, Inc.). The electrode material was prepared by grinding 7 mg Mn_5O_8 active material with 3 mg carbon black (Alfa Aesar, 99.9%) and then dissolving the mixture in DI H_2O to a concentration of 0.5 mg ml^{-1}. The resulted solution was subsequently sonicated until manganese oxide was evenly dispersed in the solution and 10 µl suspension taken by pipette (Eppendorf, Inc.) was drop-cast onto the glassy carbon working electrode (0.5 cm in diameter and 0.196 cm^2 in geometric surface area). Afterwards, the working electrode was dried in vacuum with a loading of Mn_5O_8 (3.5 µg) and carbon black (1.5 µg). Electrochemical tests were conducted in a 250 ml flat-bottom flask that contained 100 ml 0.1 M Na_2SO_4 electrolyte (Alfa Aesar, 99.9955%) in argon-purged H_2O with a rotating rate of 500 r.p.m. CV was conducted at voltage scan rates from 1 to 1,000 mV s^{-1} for six segments (three cycles) within a potential range of −1.7 to 0.8 V (versus MSE).

Symmetric two-electrode button-cells were fabricated for long-term durability and stability analyses. Each electrode for full cell tests consisted of a disk (1.5 cm in diameter, 1.77 cm^2 in area) of Toray carbon paper (E-Tek, Inc.), which was coated with ~5 mg Mn_5O_8 and 1.25 mg carbon black through drop casting. The opposing electrodes were separated via cellulose-based porous filter paper (Whatman). And each button-cell contains 200 µl 1 M Na_2SO_4 electrolyte (Alfa Aesar, 99.9955%). A stainless steel plate was placed on one side of the cell and in conjunction with a tightening bolt to ensure good electrical contact. Chronopotentiometry measurements were conducted at constant current densities from 0.5 to 50 A g^{-1} (with respective to each electrode for full cell measurements).

Data availability. The data that support the findings of this study are available from the corresponding author upon request.

References

1. Li, W., Dahn, J. R. & Wainwright, D. S. Rechargeable lithium batteries with aqueous-electrolytes. *Science* **264,** 1115–1118 (1994).
2. Chen, L., Guo, Z. Y., Xia, Y. Y. & Wang, Y. G. High-voltage aqueous battery approaching 3 V using an acidic-alkaline double electrolyte. *Chem. Commun.* **49,** 2204–2206 (2013).
3. Wang, X. J., Hou, Y. Y., Zhu, Y. S., Wu, Y. P. & Holze, R. An aqueous rechargeable lithium battery using coated Li metal as anode. *Sci. Rep.* **3,** 1401 (2013).
4. Suo, L. *et al.* 'Water-in-salt' electrolyte enables high-voltage aqueous lithium-ion chemistries. *Science* **350,** 938–943 (2015).
5. Oswald, H. R., Feitknec, W. & Wampetic, M. J. Crystal data of Mn_5O_8 and $Cd_2Mn_3O_8$. *Nature* **207,** 72 (1965).
6. Augustyn, V. *et al.* High-rate electrochemical energy storage through Li^+ intercalation pseudocapacitance. *Nat. Mater.* **12,** 518–522 (2013).
7. Liu, T. C., Pell, W. G., Conway, B. E. & Roberson, S. L. Behavior of molybdenum nitrides as materials for electrochemical capacitors - Comparison with ruthenium oxide. *J. Electrochem. Soc.* **145,** 1882–1888 (1998).
8. Kang, B. & Ceder, G. Battery materials for ultrafast charging and discharging. *Nature* **458,** 190–193 (2009).
9. Yu, X. W. & Manthiram, A. Performance enhancement and mechanistic studies of room-temperature sodium-sulfur batteries with a carbon-coated functional Nafion separator and a Na_2S/activated carbon nanofiber cathode. *Chem. Mater.* **28,** 896–905 (2016).
10. Zheng, J. M., Yan, P. F., Kan, W. H., Wang, C. M. & Manthiram, A. A spinel-integrated P2-type layered composite: high-rate cathode for sodium-ion batteries. *J. Electrochem. Soc.* **163,** A584–A591 (2016).
11. Burke, A. in *IEEE Vehicle Power and Propulsion Conference* (Chicago, IL, 2005).
12. Chen, Z. *et al.* High-performance sodium-ion pseudocapacitors based on hierarchically porous nanowire composites. *ACS Nano* **6,** 4319–4327 (2012).
13. Li, Z., Young, D., Xiang, K., Carter, W. C. & Chiang, Y. M. Towards high power high energy aqueous sodium-ion batteries: the $NaTi_2(PO_4)_3/Na_{0.44}MnO_2$ system. *Adv. Energy Mater.* **3,** 290–294 (2013).
14. Nagasubramanian, G., Jungst, R. G. & Doughty, D. H. Impedance, power, energy, and pulse performance characteristics of small commercial Li-ion cells. *J. Power Sources* **83,** 193–203 (1999).
15. Wang, X. L. *et al.* High-performance supercapacitors based on nanocomposites of Nb_2O_5 nanocrystals and carbon nanotubes. *Adv. Energy Mater.* **1,** 1089–1093 (2011).
16. El-Kady, M. F., Strong, V., Dubin, S. & Kaner, R. B. Laser scribing of high-performance and flexible graphene-based electrochemical capacitors. *Science* **335,** 1326–1330 (2012).
17. Pech, D. *et al.* Ultrahigh-power micrometre-sized supercapacitors based on onion-like carbon. *Nat. Nanotechnol.* **5,** 651–654 (2010).
18. Wu, Z. S., Parvez, K., Feng, X. L. & Mullen, K. Graphene-based in-plane micro-supercapacitors with high power and energy densities. *Nat. Commun.* **4,** 8 (2013).
19. Zhang, Z. Y., Xiao, F. & Wang, S. Hierarchically structured MnO_2/graphene/carbon fiber and porous graphene hydrogel wrapped copper wire for fiber-based flexible all-solid-state asymmetric supercapacitors. *J. Mater. Chem. A* **3,** 11215–11223 (2015).
20. Gogotsi, Y. & Simon, P. True performance metrics in electrochemical energy storage. *Science* **334,** 917–918 (2011).
21. de Groot, F. & Kotani, A. *Core Level Spectroscopy of Solids* (CRC Press Taylor & Francis Group, 2008).
22. Smith, J. D. *et al.* Energetics of hydrogen bond network rearrangements in liquid water. *Science* **306,** 851–853 (2004).
23. Wernet, P. *et al.* The structure of the first coordination shell in liquid water. *Science* **304,** 995–999 (2004).
24. Velasco-Velez, J.-J. *et al.* The structure of interfacial water on gold electrodes studied by X-ray absorption spectroscopy. *Science* **346,** 831–834 (2014).
25. Nilsson, A. *et al.* X-ray absorption spectroscopy and X-ray Raman scattering of water and ice; an experimental view. *J. Electron Spectrosc.* **177,** 99–129 (2010).
26. de Groot, F. M. F. *et al.* Oxygen 1 s x-ray-absorption edges of transition-metal oxides. *Phy. Rev. B* **40,** 5715–5723 (1989).
27. Qiao, R. *et al.* Revealing and suppressing surface Mn(II) formation of $Na_{0.44}MnO_2$ electrodes for Na-ion batteries. *Nano Energy* **16,** 186–195 (2015).
28. Qiao, R., Chin, T., Harris, S. J., Yan, S. & Yang, W. Spectroscopic fingerprints of valence and spin states in manganese oxides and fluorides. *Curr. Appl. Phys.* **13,** 544–548 (2013).
29. Jeong, D. *et al.* Mn_5O_8 nanoparticles as efficient water oxidation catalysts at neutral pH. *ACS Catal.* **5,** 4624–4628 (2015).
30. Arico, A. S., Bruce, P., Scrosati, B., Tarascon, J. M. & Van Schalkwijk, W. Nanostructured materials for advanced energy conversion and storage devices. *Nat. Mater.* **4,** 366–377 (2005).
31. Lee, J. *et al.* Unlocking the potential of cation-disordered oxides for rechargeable lithium batteries. *Science* **343,** 519–522 (2014).
32. Lukatskaya, M. R. *et al.* Cation intercalation and high volumetric capacitance of two-dimensional titanium carbide. *Science* **341,** 1502–1505 (2013).

Acknowledgements

This work was supported by the U.S. Department of Energy (DOE), Office of Science, Basic Energy Sciences under Award #DE-SC0010286 (X.T., X.S. and D.S.C.). The computation were carried out at the Extreme Science and Engineering Discovery Environment, which is supported by National Science Foundation grant number ACI-1053575 (Y.L. and G.W.). This research used resources of the Advanced Photon Source, a U.S. DOE Office of Science User Facility operated for the DOE Office of Science by Argonne National Laboratory under Contract No DE-AC02-06CH11357. The Advanced Light Source is supported by the Director, Office of Science, Office of Basic Energy Sciences, of the U.S. Department of Energy under Contract No DE-AC02-05CH11231. The neutron scattering experiments were carried out at the Spallation Neutron Source, which is sponsored by the Scientific User Facilities Division, Office of Basic Energy Sciences, U.S. Department of Energy, under Contract No DE-AC05-00OR22725 with Oak Ridge National Laboratory. This research used resources of the Center for Functional Nanomaterials, which is a U.S. DOE Office of Science Facility, at Brookhaven National Laboratory under Contract No DE-SC0012704.

Author contributions

All authors contributed to the design of the research. X.S. contributed to the material synthesis and electrochemical experimental measurements. D.S.C. contributed to X-ray and neutron PDF analysis, as well as manuscript preparation. R.Q. and W.Y. contributed to sXAS measurement. Y.L. and G.W. contributed to the theoretical analysis. D.S. contributed to TEM measurement and M.F. contributed to the neutron measurements and analysis. X.T. contributed to the manuscript preparation. All authors discussed the results and commented on the manuscript.

Additional information

Supplementary Information accompanies this paper at http://www.nature.com/naturecommunications

Competing financial interests: The authors declare no competing financial interests.

Reprints and permission information is available online at http://npg.nature.com/reprintsandpermissions/

How to cite this article: Shan, X. *et al.* Bivalence Mn_5O_8 with hydroxylated interphase for high-voltage aqueous sodium-ion storage. *Nat. Commun.* **7,** 13370 doi: 10.1038/ncomms13370 (2016).

Publisher's note: Springer Nature remains neutral with regard to jurisdictional claims in published maps and institutional affiliations.